Durable Cu-doped P3-type $Na_{0.62}Mn_{0.75}Cu_{0.19}O_2$ Cathodes for High-Capacity Sodium-ion Battery

Lunara Rakhymbay[a], Zhanar Zhakiyeva[b], Jun Ho Yu[c], A-Yeon Kim[d], Hun-Gi Jung[d,e,f], Zhansaule Bagyndyk[a], Zhumabay Bakenov[a], Seung-Taek Myung[c*], Aishuak Konarov[a*]

[a]Department of Chemical and Materials Engineering, School of Engineering and Digital Sciences, Nazarbayev University, Kabanbay Batyr Ave., 53, 010000, Astana, Kazakhstan.

[b]Core Facilities, Nazarbayev University, Astana 010000, Kazakhstan

[c]Hybrid Materials Research Center, Department of Nanotechnology and Advanced Materials Engineering, Sejong Battery Institute, Sejong University, Seoul 05006, South Korea.

[d]Center for Energy Storage Research Korea Institute of Science and Technology, Seoul 02792, South Korea

[e]KIST-SKKU Carbon-Neutral Research Center, Sungkyunkwan University, Suwon 16419, South Korea

[f]Department of Energy Science, Sungkyunkwan University, Suwon 16419, South Korea

*Corresponding author: smyung@sejong.ac.kr; aishuak.konarov@nu.edu.kz

Abstract

Sodium-ion batteries (SIBs) are currently receiving considerable attention for their prospective use in next-generation energy storage technology. Still, a primary constraint that impedes their practical application is the limited efficacy of the cathode materials. Mn-based layered oxides experience significant capacity degradation due to structural changes over cycling. Herein, this research presents a comprehensive study of the novel P3-$Na_{0.62}Mn_{0.75}Cu_{0.19}O_2$ material, elucidating the effects of partial Cu-doping on its structural and electrochemical characteristics. Our investigation employs *operando*

X-ray diffraction (XRD), demonstrating a stable single-phase reaction during the battery's cycling operation accordingly preventing P3-O3 phase transition.

Furthermore, *operando* differential electrochemical mass spectrometry (DEMS) demonstrates the absence of irreversible O_2 evolution, hence affirming the stability of reversible oxygen redox processes in this material. *Ex situ* X-ray absorption near edge structure (XANES) study reveals substantial contributions from the Cu^{2+}/Cu^{3+}, Mn^{3+}/Mn^{4+}, and O^{2-}/O^{n-} redox pairs to the overall capacity of the battery. The findings have been confirmed by X-ray photoelectron spectroscopy (XPS), which not only supports the results from the XANES investigation but also significantly enhances them. Additionally, the oxygen redox processes have been established by the obvious widening apparent in the O K-edge XANES spectra and the detection of peroxo-like oxygen species in the XPS spectra when the battery is charged to 4.7 V. The electrochemical properties of P3-$Na_{0.62}Mn_{0.75}Cu_{0.19}O_2$ material have been extensively investigated, demonstrating high capacity (212.2 mAh g^{-1} at 20 mA g^{-1}) and excellent rate performance due to the incorporation of electrochemically active Cu^{2+} ions. Finally, a full-cell of P3-$Na_{0.62}Mn_{0.75}Cu_{0.19}O_2$ with commercial hard carbon could achieve exceptional rate capability. This systematic approach highlights the key significance of Cu-doping for boosting electrochemical performance by promoting stable oxygen redox activities.

Keywords: Sodium-ion battery, Layered oxide materials, P3-type cathode, Cu doping, oxygen redox

1. Introduction

In recent years, there has been extensive research on layered oxide materials (Na_xMO_2) as a cathode for SIBs, which fulfill the criteria for affordable SIBs due to their low-cost elements and maintaining a relatively high specific capacity [1–6]. Based on the sodium content, Na_xMO_2 can be categorized into two main groups: O3-type (where $0.7 \leq x \leq 1$), which is characterized by an octahedral Na ion environment; and P-type- Na ion occupied by a prismatic site (P2 or P3 for $x \leq 0.7$) according to Delmas [7–9]. Manganese is the key supporting element in the structure of most of these layered oxides, due to its low cost, nontoxicity, range of oxidation states, and structure-promoting properties. The Mn^{3+}/Mn^{4+} redox couple can be operated efficiently, however, for achieving high

energy density in practice, the active redox couple of $Ni^{2+}/Ni^{3+}/Ni^{4+}$ or Fe^{3+}/Fe^{4+} is required, with Mn^{4+} predominantly serving a passive role [10–13]. Nonetheless, Mn-based LTMOs suffer from unresolved issues which are associated with Jahn-Teller distortion due to the presence of Mn^{3+} ion and the dissolution of inactive Mn^{2+} at the interface between the cathode and electrolyte at the end of discharge[14]. The occurrence of Jahn-Teller distortion exhibits a change of Mn-O distances in the structure through the z-axis. The combination of the above-mentioned factors results in several phase transformations, as well as in fast capacity deterioration and consequently substantial loss of the layered crystal structures[15]. Additionally, Mn vacancies were identified in Na_xMO_2, which probably formed as a result of oxygen absorption and the gradual cooling-induced oxidation of the Mn trivalent[16]. Over the past decades, potential solutions to these mentioned issues in P2 and O3-type layered materials were the partial replacement of Mn with other low-valence electrochemically active/non-active cations such as Li[17,18], Ni[15,19], Mg[20–22], Co[23,24], Fe[25], and Al[26]. They work by mitigating the aberrant elongation of Mn-O along the z-axis within the MnO_6 octahedra and by decreasing the concentration of Mn^{3+} which leads to improved cycle stability and structure stabilization compared to pristine ones [15]. Moreover, scientists are attracted by the possibility of enhancing the electrochemical capacity of cathodes by anionic redox activity in Mn-based transition metal oxide materials. This approach along with doping presents a promising opportunity by storing charges on the oxygen ions. When replacing certain transition metals in the transition metal layer with non-TMs, or TMs with a completely filled d-shell, the metal-oxygen bond breaks or turns less directed, which eases the formation of a peroxo-like O–O bond to have the ability to form [27]. In order to induce the oxygen activity the general configuration of Na–O–A, represented by the formula $Na[A_xTM_{1-x}]O_2$, where A is active/inactive cations, is used [28]. For instance, our group previously reported the consequences of Zn doping on P2-type $Na_{2/3}[Mn_{1-x}Zn_x]O_2$ throughout an extensive range of $0 \leq x \leq 0.3$. The O^{2-}/O^{n-} reversible redox reaction was observed by Zn substitution at Mn sites. Furthermore, the cycling performance of the P2-$Na_{2/3}[Mn_{0.7}Zn_{0.3}]O_2$ material was significantly improved with 80% capacity retention [29]. Cheng et al. investigated comprehensive Al-doping on P2-$Na_{0.6}Ni_{0.3}Mn_{0.7}O_2$ which demonstrated that the aluminum enhances the reversible oxygen redox reactions by facilitating the reductive coupling processes between unpaired oxygen (O) 2p states in

localized Na-O-Al[11]. According to Yabucchi et al., P2-type $Na_{2/3}[Mg_{0.28}Mn_{0.72}]O_2$ exhibits a high 200 mAh g^{-1} reversible capacity at 1.5-4.4 V by oxygen redox [20]. Armstrong's group demonstrated the ability to undergo oxygen redox reactions at high potentials of P3-$Na_{0.67}Ni_{0.2}Mn_{0.8}O_2$ which delivered a significant initial discharge capacity of 204 mAh g^{-1}. The outcomes indicated that reducing Ni stabilizes anionic redox activity due to robust Ni 3d−O 2p hybridization states over the charge [30].

Mn-based layered compounds have recently shown electrochemical activity in the Cu^{2+}/Cu^{3+} redox due to the applicability of high working voltage and good capacity retention achievable in comparison with copper-substitution in LIBs [12]. Owing to its comparatively smaller ionic radius (0.73 Å) in comparison to sodium (1.02 Å), copper exhibits the potential to serve as a partial substitute for transition metals within TMO_2 layers [31]. According to theoretical and practical research, it has been proposed that Cu-doping for Mn in $NaMnO_2$ stabilises the β-phase. This replacement promotes the presence of Mn in its tetravalent oxidation state and Cu in its divalent oxidation state [32]. In addition, in the Na-Mn-Cu-O system, an anionic redox reaction can be initiated during the high-voltage charging rather than deterioration of the structure [33]. For instance, Zheng et.al studied oxygen redox activity with minimal voltage hysteresis at the layered $Na_{0.67}Cu_{0.28}Mn_{0.72}O_2$ cathode and demonstrated that the oxygen redox activity is enhanced by the non-bonding O 2p states along the Cu-O bond. P2-$Na_{0.67}Cu_{0.28}Mn_{0.72}O_2$ revealed a remarkably reversible capacity of 104 mAh g^{-1} with a consistent voltage profile leading to cationic and anionic redox mechanisms [27]. Later on, Komaba et al. showed a comprehensive investigation on the consequences of Cu-substitution for Mn in P′2- and P2-type $Na_{0.67}[Cu_xMn_{1-x}]O_2$, ($0 < x \leq 0.33$) with an emphasis on the synergistic Jahn−Teller distortion of Mn^{3+} and Cu^{2+} ions, featuring reversible redox reactions of $Mn^{3+}/^{4+}$, $Cu^{2+}/^{3+}$, and O^{2-}/O^{1-}. The activation of oxygen redox is unaffected by the type of Mn substituent, according to a comparison. On the other hand, the structure changes during charge/discharge depending on the nature and content of substituent elements. In response to this, the P2-type $Na_{0.67}[Cu_xMn_{1-x}]O_2$ keeps its P2 phase without any additional phases during the bulk and at the end of the charge (at 4.5 V), which prevents O_2 voltage hysteresis [34].

Prior research has mostly addressed Cu-substituted P2-type sodium-layered manganese oxides, even though P3-type materials may be seen as more environmentally friendly due to their ability to synthesize at lower temperatures. Considering that the c parameter and d-spacing values are larger than P2 and O3, which facilitate better sodium diffusion; nonetheless, potentially causing structural instability [35]. The rapid capacity fading in P3-type materials is assumed to be caused by one of the various reasons behind the phenomenon. Linnel et al. conducted a study impact of Cu-doping to comprehend the oxygen redox activity in P3-type layered oxide materials. P3-$Na_{0.67}Mn_{0.9}Cu_{0.1}O_2$ delivered a higher capacity of 176.3 mAh g^{-1} over the wide voltage window of 1.8–4.3 V, even so, cycling performance had a sharp drop where maintained only for retention of 71% after 40 cycles. Deformation of the P3 phase to the P′3 phase during charging to 4.3 V, and subsequently a full phase transition of P′3→O′3 upon discharge to 1.8 V, which relates to the capacity fading [36]. Despite this, the high capacity that can be obtained in the P3-type compound is still desirable. More P3-type materials with anionic redox activity are being investigated, however the intrinsic mechanism is still being debated.

Inspired by the previous works involving copper-substituted cathode materials, we conducted a detailed investigation of P3-$Na_{0.62}Mn_{0.75}Cu_{0.19}O_2$ to assess how partial Cu-doping influences its structural and electrochemical properties. Our study utilizes operando X-ray diffraction (XRD), which reveals a consistent single-phase reaction throughout the battery's cycling process. Additionally, operando differential electrochemical mass spectrometry (DEMS) indicates the absence of irreversible O_2 evolution, confirming the stability of reversible oxygen redox reactions in this compound. Further insights are provided by ex situ X-ray absorption near edge structure (XANES) analysis, which shows significant contributions from Cu^{2+}/Cu^{3+}, Mn^{3+}/Mn^{4+}, and O^{2-}/O^{n-} redox pairs to the battery's total capacity. These findings are corroborated by X-ray photoelectron spectroscopy (XPS), which not only confirms the results from the XANES study but also enriches them. Particularly, oxygen redox processes are verified by the notable broadening observed in the O K-edge XANES spectra and the identification of peroxo-like oxygen species in the XPS spectra when the battery is charged up to 4.7 V. This comprehensive approach underscores the pivotal role of Cu-doping in enhancing electrochemical performance by facilitating stable oxygen redox activities.

2. Experimental section

2.1 Materials

Sodium nitrate ($NaNO_3$, 99.5%), manganese (II) carbonate ($MnCO_3$, 99 %), and copper oxide (CuO, 99%) and N-methyl pyrrolidone were purchased from Sigma-Aldrich, USA and polyvinylidene fluoride (PVdF) and acetylene black (AB) were sourced from MTI Corp., Richmond, USA. All reagents were analytical grade and used directly without further treatment.

2.2 Materials synthesis

$Na_{0.62}Mn_{0.75}Cu_{0.19}O_2$ material was prepared by a simple solid-state method: a stoichiometric amount of sodium nitrate, manganese carbonate, and copper oxide were homogeneously ground for 15-30 minutes in agate mortar with a proper amount of acetone and further pressed into tablets with 20 mm diameter. The tablets were calcined in an oxygen atmosphere at 600°C at a rate of 10°C/min for 5 hours with subsequent natural cooling. Before material characterization, the as-synthesized materials were stored in a vacuum desiccator.

2.3 Characterization

X-ray diffraction (XRD) measurements were carried out with a benchtop MiniFlex (Rigaku, Nazarbayev University) in a 2θ range of 10 to 70º. The obtained XRD data were refined using the FullProf program. The sample morphologies were observed using scanning electron microscopy (SEM) (Crossbeam 540, Zeiss, Core Facilities, Nazarbayev University). NEXSA XPS spectrometer equipped with an Al Ka achromatic X-ray source (1486.6 eV) was used to define the oxidation states of the elements (Core Facilities, Nazarbayev University). The high-resolution transmission electron microscopy (HRTEM, JEM-3010, JEOL, Sejong University, South Korea) with energy-dispersive X-ray spectroscopy (7200-H, HORIBA, Sejong University, South Korea) was used to determine crystal morphologies and elemental analysis. The chemical compositions of the as-synthesized powders were analyzed by inductively coupled plasma–atomic emission spectroscopy (ICP-AES, Optima 8300, Perkin-Elmer, Sejong University, South Korea) and X-ray Fluorescence (PanAnalytical, ICGM,

France). Structural studies during cycling were performed using *operando* XRD (X'Pert, PANalytical diffractometer, 14–50° (2θ) Sejong University, South Korea). XAS analyses for the Mn and Cu K-edge regions were performed in a transmission mode, and the O K-edge measurements in a fluorescence mode at the 8C beamline (Pohang Accelerator Laboratory (PAL), South Korea). The obtained XAS data were analyzed using the Athena software program [37].

2.4. Electrochemical measurements

$Na_{0.62}Mn_{0.75}Cu_{0.19}O_2$ powder was mixed with acetylene black and polyvinylidene fluoride (PVdF) binder in a ratio of 8:1:1 (wt.%) in N-methyl-2-pyrrolidone (NMP). The homogeneous mixtures were applied on aluminum (Al) foil using a doctor blade and then dried overnight at 80°C in a vacuum oven. The mass loading of the active materials was ≈ 3.5-4 mg cm^{-2}. The $Na_{0.62}Mn_{0.75}Cu_{0.19}O_2$ electrodes were paired with Na metal in CR2032 coin-type cells, glass fiber separators (AGM), and electrolyte, 0.5M $NaPF_6$ in propylene carbonate (PC) and fluoroethylene carbonate (FEC) (98:2 by volume). The electrochemical test was performed by applying a constant current of 20 mA g^{-1} (0.1C) in a voltage range of 1.5 – 4.7 V on a WonAtech BTS at an ambient temperature. Galvanostatic intermittent titration technique (GITT) measurements were performed with 5 minutes of charge and discharge, followed by relaxation periods of 5 min at a current density of 0.1C (20mA g^{-1}). *Operando* differential electrochemical mass spectrometry (*o*-DEMS) was performed in an R2032 coin-type cell utilizing HPR-40 DEMS, a Hidden Analytical instrument. The commercial hard carbon was used as an anode for full cell. The N/P ratio was 1.2.

3. Results and discussion

3.1 Structural and morphological characterizations

A series of Cu-doped $Na_{0.62}Mn_{1-x}Cu_xO_2$ (x=0, 0.09, 0.19, and 0.28) materials were synthesized using a simple solid-state method. The chemical compositions of as-synthesized $Na_{0.62}Mn_{1-x}Cu_xO_2$ were evaluated by ICP-AES and XRF measurements. The results are summarized in Table S1-S2, which shows an accurate match with the designed chemical composition, indicating the successful synthesis of the samples. However, there are observed deviation in the total metal content, which not

equal to one (Mn + Cu ≠ 1). But, the noticed Mn deficiency likely results from the formation of metal vacancies which are known to undoped material system ($Na_{0.62}MnO_2$) where Mn vacancies enable non-bonding 2p oxygen orbitals to deliver an additional capacity through oxygen redox [38].

The crystal structure and phase composition were investigated by the X-ray diffraction (XRD) patterns and accompanying Rietveld refinements of $Na_{0.62}Mn_{1-x}Cu_xO_2$ as presented in Fig. 1a and Fig. S1. The XRD patterns of the samples exhibit diffraction peaks that can be attributed to the predominant P3-type layered structure with the R-3m space group with a small presence of the P1 triclinic phase as presented in Fig.1a. According to quantitative phase analysis, the ratio between minor triclinic and P3 phases comprises only 6.6 : 93.4 %. Rietveld refinements were performed using the FullProf software. Fig. 1a clearly illustrates that the $Na_{0.62}Mn_{0.75}Cu_{0.19}O_2$ material does not include the CuO or any other impurities. The refined cell parameters for $Na_{0.62}Mn_{0.75}Cu_{0.19}O_2$ were a=2.8807 Å, b=2.8807 Å, and c = 16.7313 Å and detailed refined data are presented in Tables S3 and S4. As shown in the crystal structure representation (Fig.1b), the oxygen slabs follow the ABBCCA stacking sequence typical of P3-type materials. Between the three compounds, $Na_{0.62}Mn_{0.75}Cu_{0.19}O_2$ is chosen to undergo a comprehensive structural investigation.

The morphology of prepared $Na_{0.62}Mn_{0.75}Cu_{0.19}O_2$ was analyzed by SEM (Fig.1c). The materials have a distinct hexagonal structure characterized by very tiny irregular-shaped particles with unclear edges, which align with the typical layered structure material. The small particle size improves electrochemical performance by shortening Na+ pathways, increasing surface area, and thereby improving particle interaction[39]. Although the particle morphology seems irregular at the macroscopic level, the interior crystallographic structure displays the distinct layered order typical of P3-type materials as shown in HR-TEM results (Fig.1d). Its electrochemical performance depends on its ordered structure, which enhances Na+ diffusion. HR-TEM image revealead a distinct uniform lattice fringe with a length of 0.553 nm. This fringe corresponds to the d-spacing value of the (003) plane in the P3 phase, which is in good agreement with the selected area electron diffraction (SAED) pattern. The ring SAED pattern (Fig.1e) identifies (003) and (006) corresponding planes indicating a correlation with structure refinement. The EDS mappings illustrated in Fig.1f demonstrate a

homogeneous dispersion of Na, Mn, Cu, and O inside the bulk phase, implying that Cu has played a role in the crystallization process across the entirety of the component.

3.2 Electrochemical performance

Electrochemical performances of Cu-doped $Na_{0.62}Mn_{1-x}Cu_xO_2$ cathode materials were examined in Na half-cell configuration at 25°C. As shown in Fig.2a and Fig. S3, cathode materials was measured in the voltage window of 1.5 – 4.7 V at a constant 20 mA g^{-1} current density to show the electrochemical behavior for the first five cycles. P3-$Na_{0.62}Mn_{0.75}Cu_{0.19}O_2$ exhibits an initial charge and high discharge capacity of 148.5 mAh g^{-1} (0.55 Na^+: $Na_{0.07}Mn_{0.75}Cu_{0.19}O_2$) and 212.2 mAh g^{-1} (0.79 Na^+: $Na_{0.86}Mn_{0.75}Cu_{0.19}O_2$), respectively. A noticeable difference in the voltage profile can be seen following the first cycle. The inability of Mn^{4+} to undergo additional oxidation state in $Na_{0.62}Mn_{0.75}Cu_{0.19}O_2$ during Na+ deintercalation is ascribed to a reversible oxygen-redox mechanism [38]. Nevertheless, there was a slight fading in the capacity throughout the cycles. Coexistence of triclinic phase is defined by intrinsic lattice distortion, attributed to Mn-vacancy in their structure that induce stress inside during desodiation/sodiation [40,41]. The undoped sample material displayed an initial discharge capacity of 186.14 mAh g^{-1}. Nonetheless, performance immediately deteriorated, with substantial capacity loss evident during the initial five cycles (Fig. 2b).

Differential capacity profiles in Fig. S2 shows one sharp oxidation peak at 4.5 V, further peak at 3.6-4.2V and reversible reduction peaks at 3.6-4V, 3.0V and 2.0 V which corresponding to the redox of Mn^{4+}/Mn^{3+}, Cu^{2+}/Cu^{3+}, and O^{2-}/O^{n-}, respectively during the first cycle. It became apparent that following the first cycle, the dQ/dV curves exhibited a significant reduction in peak intensity, indicating smoother plateaus with fewer distortions. On the other hand, this behavior can be attributed to the presence of Cu ion in the structure, which suppresses the Jahn-Teller distortion by reducing concentration of Mn^{3+}. As prior studies have proved, the incorporation of Cu^{2+} into the crystal structure lowers the number of Mn^{3+} ions thereby it raises the quantity of Mn^{4+} to balance charges. This structural stabilization is identified in the reduced distortion ratio between Jahn-Teller active (Mn^{3+}, Cu^{2+}) and inactive (Mn^{4+}) species [34]. More importantly, the irreversible oxidation peak at ~4.5 V (is seen inset of dQ/dV plots) disappeared upon 5th cycles. The nature of anionic redox has been

extensively studied for layered oxides that investigated the activity of formation of superoxo-related and peroxo-related species during charging. The superoxo-related species is particularly significant because they are unstable and prone to reacting with the electrolyte solvent, such as propylene carbonate (PC), resulting in parasitic products from solvent breakdown further contributing to capacity fading [42–44]. There may be a significant possibility of the disappearance of the oxidation peak at ~4.5 V over subsequent cycles aligns with these findings.

The cycling performance of P3-$Na_{0.62}Mn_{0.75}Cu_{0.19}O_2$ is shown in Fig.2c at rates of 20 mA g^{-1} and 100 mA g^{-1}, respectively. After five cycles of activation at low current density, the material exhibits a slight fading. Certainly, the material has good cycling showing no noticeable decrease in capacity even after undergoing 30 cycles with 87% capacity retention. Rate capabilities of the P3-$Na_{0.62}Mn_{0.75}Cu_{0.19}O_2$ at current densities 20, 40, 100, 200, 400, and 1000 mA g^{-1} are examined and shown in Fig.2d. Specifically, depending on the rate capability the capacity varies from 205.8 mAh g^{-1} at a 20 mA g^{-1} to 140.4 mAh g^{-1} at a 200 mA g^{-1} discharge rate. Even with a high-rate of 1000 mA $g^{-1,}$ the sodium half-cell consisting of the P3-$Na_{0.62}Mn_{0.75}Cu_{0.19}O_2$ cathode still supplies an acceptable reversible capacity of 88.3 mAh g^{-1}. The rate performance shows that the capacity decreases stepwise as the current gradually increases, and it recovers to a high level when the current density returns to the initial value of 20 mA g^{-1}, which indicates a strong capability for capacity recovery.

The galvanostatic intermittent titration technique (GITT) was applied to further characterize the electrodes to evaluate the kinetics of Na+ diffusion of $Na_{0.62}Mn_{0.75}Cu_{0.19}O_2$. The cell was tested at a constant current flux (20 mA g^{-1}) between 1.5- 4.7 V during the second charge and discharge (Fig.2e). The collected data can be put to use in the Fick's second law equation to derive the associated diffusion coefficients:

$$D_{Na+} = \frac{4}{\tau\pi}\left(\frac{m_B V_M}{M_B A}\right)^2\left(\frac{\Delta E_s}{\Delta E_\tau}\right)^2 \qquad (1)$$

where, τ, m_B(g), V_M ($cm^3\,mol^{-1}$), M_B (g mol^{-1}), and A (cm^2) are identified as pulse duration, the active mass of the electrode, molar volume, and molar mass of the $Na_{0.62}Mn_{0.75}Cu_{0.19}O_2$ and surface area of

electrode respectively. ΔE_s and ΔE_τ represent a difference between steady-state potential (V) and potential change throughout the current pulse excluding the IR drop (V), correspondingly. The calculated Na+ diffusion coefficients are shown in Fig.2f. Typically, D_{Na+} values normally vary between $2.6763*10^{-7}$ to $2.1503*10^{-10}$cm^2 s^{-1}. In addition, a log value is performed to identify minor fluctuations in D_{Na+}. Generally, during the discharge cycle one sharp and one weak region can be identified which corresponds to the vacancy-cation ordering at ~3.0 V and for the $Mn^{4+/3+}$ at ~2.1-2.5 V [44]. However, during the charge process, the region is not identified. These can be associated with non-occurring polarization above 4.2 V after Cu-doping resulting in prevented phase change to O3 as with high potential polarization possible to the existence of O-type stacking, which enhances the Na+ diffusion barrier. As observed in the low voltage area, small polarization can be the consequence of Jahn-Teller-induced phase transformation due to the increasing Mn^{3+} concentration at the end of discharge [34,45].

Further, for consideration of the practical efficacy of cathode material the full cell was designed with commercial hard carbon anode. The both electrodes were pre-cycled for 3 cycles at 20 mA g^{-1} in order to achieve stable profiles before full cell assembling [46] (Fig 3a). The ideal N/P ratio based on weight of cathode and anode was figured out as 1.2. The full cell demonstrated an esteemed 178 mAh g^{-1} capacity at the first cycle at 20 mAhg^{-1} in cut-off voltage range of 1.2-4.4 V (Fig 3b). The rate performance of full cell also was highlighted at different current densities (20, 40, 100, 200 and 400 mA g^{-1}). While at a high current density, the capacity of the full cell continues to reach 50 mAh g^{-1}. Furthermore, the full cell keeps demonstrating reversible capacity capability (Fig 3c).

3.3 Structure evaluation

In order to examine the change in oxidation states in our materials upon charge/discharge cycles the XANES (Fig. 4) and XPS (Fig. 5 and Fig S.5) have been performed. Fig. 4a shows Cu K-edge spectra for P3-$Na_{0.62}Mn_{0.75}Cu_{0.19}O_2$ and a standard reference for Cu^{2+} oxidation state. Copper in our pristine sample

is divalent as inferred by the comparison with the CuO standard. Upon charge to 4.7 V, the intensity of the Cu K-edge spectrum decreases slightly. The most profound change is observed at the shoulder region at about 8990 eV. The flattening of the shoulder (indicated by an arrow on Fig. 4a) implies the oxidation of Cu^{2+} to Cu^{3+} state [35] . We note, however, that the above-discussed changes in Cu K-edge spectra upon charge can be explained by the influence of oxygen ligands bonded to copper metal. The oxidation of these O^{2-} leads to the different Cu-O and O-O bond lengths and thus geometry, which might consequently affect the shape of Cu K-edge spectrum. The Cu 2p XPS spectra of a pristine material (Fig. 5a) indicates that Cu is in the oxidation state 2+. The signal features two typical peaks of Cu 2p1/3 and Cu 2p2/3 at binding energies of 935 and 955 eV, respectively, with characteristic satellites (only one shown). A slight shift to higher energies upon charging to 4.7 V of $Na_{0.62}Mn_{0.75}Cu_{0.19}O_2$ shows that Cu^{2+} undergoes oxidation to higher oxidation state complementing our Cu K-edge XAS information (Fig.4a). As expected, upon full discharge to 1.5 V the peaks return to Cu^{2+} state as observed in the pristine material.

Fig. 4b shows all collected Mn K-edge spectra for $Na_{0.62}Mn_{0.75}Cu_{0.19}O_2$ and standard references for $Mn^{3+}$and Mn^{4+}, respectively. Based on the qualitative comparison between the standard references and the pristine material, the valence state of the latter is close to tetravalent [45], but not exactly Mn^{4+}. Upon charge to 4.7 V there is a slight shift to higher energies indicating the oxidation of a pristine sample to Mn^{4+}, which can be inferred by the comparison with a reference MnO_2 sample. The Mn K-edge spectrum of the discharged P3-$Na_{0.62}Mn_{0.75}Cu_{0.19}O_2$ shifts significantly (by about 4 eV) to lower energies, which is attributed to Mn reduction to 3+ state and extra Na+ insertion. The Mn XPS spectra of P3-$Na_{0.62}Mn_{0.75}Cu_{0.19}O_2$ samples are shown on Fig.5b and 5c. The XPS energy ranges for both Mn 2p (Fig.5b) and Mn 3s (Fig.5c) have been probed. Generally, Mn 3s peaks are used to identify the oxidation states of Mn, with ΔMn 3s decreasing with rising oxidation states (4.4 eV < 5.4 eV < 6.1 eV for Mn^{4+}, Mn^{3+}, Mn^{2+}, respectively). The ΔMn 2p generally follows the same trend, with lower delta signifying higher oxidation states. However, Mn 2p is less reliable due to very close-lying doublet peaks for Mn^{2+}, Mn^{3+} and Mn^{4+}

states. In the pristine sample, the ΔMn 3s is ~5 eV, suggesting the simultaneous presence of Mn^{3+} and Mn^{4+}. The ΔMn 2p has a value of ~11.8 eV which matches the reported values for MnO2 (11.8 eV), indicating the presence of Mn in a tetravalent oxidation state. The Mn 2p and Mn 3s XPS spectra for the charged state indicate the Mn^{4+} state. Upon discharge the Mn 2p peaks shift to lower energies signaling the presence of Mn^{3+} species.

The oxygen K-edge spectra were collected for pristine, half-charged, fully charged, half-discharged, and fully discharged samples (Fig.4c). The general features of oxygen redox were observed, with the spectra below 533 eV revealing absorption peaks at ~529 and ~531.5 eV. The two latter peaks can be explained by the electronic transitions from the O 1s states to unoccupied hybridized O 2p-transition metal t_{2g} and e_g states, respectively [36,47,48]. Widening of the spectra and an increase in the e_g peak intensity with a shift to higher energies is observed upon charging to 4.7 V. Upon discharge to 1.5 V, the reverse changes take place: the overall narrowing of the spectra and lowering of the e_g peak intensity with a shift to lower energies. We assign these changes to a reversible oxygen redox [49]. The O 1s XPS spectra of the P3-$Na_{0.62}Mn_{0.75}Cu_{0.19}O_2$ in a pristine state exhibit three clearly identifiable peaks (Fig. S5): oxygenated carbonated species (C=O and C−O) at ~ 532.0 eV and ~ 535.0 eV, respectively; and the lattice oxygen (O^{2-}) peak at ~ 530.0 eV; Upon charge indicates the presence of an extra small peak at ~ 530.4 eV, identified as the peroxo-like oxygen (O^{2n-}) emerges throughout the charging process (Fig.S5)[49,50]. The existence of the latter suggests possible oxygen redox activity during the first charging process [51,52].

Operando differential electrochemical mass spectrometry (DEMS) was applied to investigate the oxygen dynamics of $Na_{0.62}Mn_{0.75}Cu_{0.19}O_2$ throughout the charging process. Fig.6 indicates that no detectable O_2 release occurred in the high-voltage region, implying an absence of notable oxygen evolution. This data corroborates the assumption of a reversible anionic redox mechanism (O^{2-}/O_2^{n-}); however, it does not exclude the potential for modest structural alterations or other oxygen-related activities that may not lead to observable O_2 evolution. In sodium layered oxides, irreversible oxygen

evolution processes ($O^{2-}/O_2^{n-}/O_2$) are commonly seen and are typically attributed to the movement of manganese ions and the subsequent reconfiguration of manganese and vacancies inside the TMO_2 planes during charging [40,53].

In order to investigate the crystal structure evolution and the phase transition of $Na_{0.62}MnO_2$ and $Na_{0.62}Mn_{0.75}Cu_{0.19}O_2$ an *operando* XRD was carried out at a voltage range of 1.5 to 4.7 V upon the first Na^+ desodiation/sodiation. The Fig.7a presents the contour map evolution of the structure during charge/discharge on the right side while the corresponding voltage profile is depicted from the left side. As is readily observed from the contour map, the initial desodiation stage does not result in the formation of any new peaks, and the P3 layered structure is maintained throughout the full charge/discharge process. The observed result suggest a solid-solution behavior upon charging to 4.7 V and subsequent discharging to 1.5 V. Moving of the peak positions in a reversible manner can be influenced by of the relative amount of sodium [48]. At the initial stages of Na+ extraction, the values for (003) and (006) reflections continuously monotonic migrate towards smaller angles, showing an increase in the lattice parameter c. The observed pattern was confirmed by calculating a variation in lattice parameter during full charge/discharge process applying the least squares approach as illustrated in Fig.7b where charging caused a raise of c lattice parameter value and dropping of a,b parameters. With the resulting shift being reversible subsequent discharge. It was explained by an enhanced repulsive contact of oxygen ions during the Na+ deintercalation process between the neighboring layers[50,51]. Generally, lattice parameter changes in layered cathodes influenced by shifts in TM and metal layers. When sodium is removed from the structure, the shielding effect between the oxygen layers is reduced, which causes an increase in repulsion and a wider distance in the layers. The a lattice parameter decreases as the transition metal layer volume decreases during charging and the c lattice parameter increases due to a more pronounced alteration in the spacing of the sodium layer [52]. Meanwhile, the (101) and (012) patterns exhibit a shift towards higher angles. It is important to highlight that the volume change showed only showed a 1.54% (Fig.7b).

Furthermore, there are no additional peaks, which suggests that a substantial suppressive effect on phase transitions from the hexagonal P3 phase to the O3 and O3′ phases at high voltage. Generally, anisotropy variations in transition TM-O bonding during charge and discharge are associated with phase transitions in cathode materials. Robust Cu-O covalence promotes the stability of the TM-O structure, suppressing phase transitions and preserving lattice integrity, corresponding with prior studies [54–56]. Because of this stabilization, TMO_2 layer gliding is reduced, which in turn minimizes volume changes and stress creation [56]. The XRD data for the undoped electrode (Fig. S7) indicates considerable shifts of the 15.8°and 32.2° 2θ peaks towards higher angles throughout the Na+ extraction in the charging process. These alterations signify a volumetric change resulting from the gliding of $[\square 1/7Mn6/7]O_2$ layers, as observed in prior research [40]. Following discharge to 1.5 V, this voltage range coincides with the Mn^{4+}/Mn^{3+} redox reaction. This indicates that the redox activity of Mn is intricately linked to structural changes resulting from Jahn-Teller distortion, which involves phase separation and the development of biphasic domains. This mechanism is additionally corroborated by the XRD plots (Fig. S7), where the most prominent peaks diminish in intensity, and two new peaks arise, indicating a splitting of the primary peak becoming unstable. The new peaks are attributed to P'2 phases (Fig. S7) [44,57]. Further *ex situ* XRD was conducted for the first charge and discharge to additional investigate structural evolution. The XRD pattern of fresh electrode exhibiting characteristics P3 phase peaks (Fig. S9). Upon charging the electrode to 4.7 V, most of peaks associated with the P3 phase remain observable. Nonetheless, there is a continuous decrease of intensities. This suggests possibly due to more sodium removal, which disrupts atomic arrangement within the lattice [53]. The following material was discharged to 1.5 V, obtained diffraction indicated P3 structure phase. Moreover, *ex situ* XRD patterns provided (Fig.S10) to be able to conduct further investigations into the structural development after 30 cycles. As revealed, we observed that the structure could be maintained after 30 cycles.

4. Conclusion

In summary, the novel P3-$Na_{0.62}Mn_{0.75}Cu_{0.19}O_2$ material exhibits substantial potential as a cathode for sodium-ion batteries. An impressive initial charge capacity of 143 mAh g^{-1} was realized, attributed to the redox activity of $Cu^{2+}/^{3+}$ and $O^{2-}/^{n-}$ pairs. During discharge, the material delivered an exceptional capacity exceeding 200 mAh g^{-1}, facilitated by the redox pairs $Cu^{3+}/^{2+}$, $Mn^{4+}/^{3+}$, and $O^{2-}/^{n-}$. These redox pairs continued to actively participate in subsequent cycles, ensuring sustained performance. The robustness of these findings was validated through a combination of *ex situ* X-ray absorption spectroscopy (XAS), X-ray photoelectron spectroscopy (XPS), and *operando* differential electrochemical mass spectrometry (DEMS) measurements. The incorporation of partial Cu-substitution significantly enhanced structural stability during cycling, as evidenced by *operando* X-ray diffraction (XRD) data, which consistently indicated a single-phase reaction. Moreover, the Cu-substitution effectively mitigated the Jahn-Teller distortion associated with Mn^{3+}, contributing to overall stability. This comprehensive study highlights the pivotal role of Cu-doping in enhancing the electrochemical performance of sodium-ion batteries by stabilizing oxygen redox activities and improving structural integrity.

Conflicts of interest

There are no conflicts to declare

CRediT authorship contribution statement

L. R.: Writing – original draft, Visualization, Validation, Investigation, Data curation. **J. H. Y.**: Validation, Investigation, Data curation, **Zh. Zh.**: Investigation, Data curation, Validation, Review& Editing, **Zh. B.:** Data curation, Methodology, Validation, **A-Y. K., H.-G. J.**: Data curation, Methodology, Validation, **Z. B.**, **S.-T. M.**: Conceptualization, Visualization, Validation, Review & editing, **A. K.**: Conceptualization, Visualization, Validation, Writing – review & editing, Supervision, Funding acquisition.

Acknowledgments

This work is funded by Nazarbayev University under Collaborative Research Program Grant №20122022P1611, AK and under Faculty-development competitive research grants program for 2024-2026 Grant №201223FD8802, AK.

References:

1 J.-Y. Hwang, S.-T. Myung and Y.-K. Sun, *Chem. Soc. Rev.*, 2017, **46**, 3529–3614.
2 N. Yabuuchi, K. Kubota, M. Dahbi and S. Komaba, *Chem. Rev.*, 2014, **114**, 11636–11682.
3 E. Goikolea, V. Palomares, S. Wang, I. R. De Larramendi, X. Guo, G. Wang and T. Rojo, *Advanced Energy Materials*, 2020, **10**, 2002055.
4 C. Delmas, *Advanced Energy Materials*, 2018, **8**, 1703137.
5 B. Shugay, L. Rakhymbay, A. Konarov, S.-T. Myung and Z. Bakenov, *Electrochemistry Communications*, 2023, **146**, 107413.
6 N. Voronina and S.-T. Myung, *Energy Material Advances*.
7 N. Voronina, J. H. Yu, H. J. Kim, N. Yaqoob, O. Guillon, H. Kim, M. Jung, H. Jung, K. Yazawa, H. Yashiro, P. Kaghazchi and S. Myung, *Adv Funct Materials*, 2023, **33**, 2210423.
8 L. Yang, S. Luo, Y. Wang, Y. Zhan, Q. Wang, Y. Zhang, X. Liu, W. Mu and F. Teng, *Chemical Engineering Journal*, 2021, **404**, 126578.
9 S. Birgisson, T. L. Christiansen and B. B. Iversen, *Chem. Mater.*, 2018, **30**, 6636–6645.
10 X. Ma, H. Chen and G. Ceder, *J. Electrochem. Soc.*, 2011, **158**, A1307.
11 C. Cheng, M. Ding, T. Yan, J. Jiang, J. Mao, X. Feng, T. Chan, N. Li and L. Zhang, *Small Methods*, 2022, **6**, 2101524.
12 C. W. Mason, F. Lange, K. Saravanan, F. Lin and D. Nordlund, *ECS Electrochemistry Letters*, 2015, **4**, A41–A44.
13 N. Voronina, H. J. Kim, A. Konarov, N. Yaqoob, K.-S. Lee, P. Kaghazchi, O. Guillon and S.-T. Myung, *Advanced Energy Materials*, 2021, **11**, 2003399.
14 J. Wang, H. Liu, Q. Yang, B. Hu, F. Geng, C. Zhao, Y. Lin and B. Hu, *ACS Appl. Mater. Interfaces*, 2020, **12**, 34848–34857.
15 A. Konarov, J. U. Choi, Z. Bakenov and S.-T. Myung, *J. Mater. Chem. A*, 2018, **6**, 8558–8567.
16 H. Liu, X. Gao, J. Chen, J. Gao, H. Wang, Y. Mei, H. Liu, W. Deng, G. Zou, H. Hou and X. Ji, *Journal of Energy Chemistry*, 2022, **75**, 478–485.
17 N. Yabuuchi, R. Hara, M. Kajiyama, K. Kubota, T. Ishigaki, A. Hoshikawa and S. Komaba, *Advanced Energy Materials*, 2014, **4**, 1301453.
18 E. De La Llave, E. Talaie, E. Levi, P. K. Nayak, M. Dixit, P. T. Rao, P. Hartmann, F. Chesneau, D. T. Major, M. Greenstein, D. Aurbach and L. F. Nazar, *Chem. Mater.*, 2016, **28**, 9064–9076.
19 Z. Lu and J. R. Dahn, *Journal of The Electrochemical Society*.
20 N. Yabuuchi, R. Hara, K. Kubota, J. Paulsen, S. Kumakura and S. Komaba, *J. Mater. Chem. A*, 2014, **2**, 16851–16855.
21 J. Billaud, G. Singh, A. R. Armstrong, E. Gonzalo, V. Roddatis, M. Armand, T. Rojo and P. G. Bruce, *Energy Environ. Sci.*, 2014, **7**, 1387–1391.
22 R. J. Clément, J. Billaud, A. Robert Armstrong, G. Singh, T. Rojo, P. G. Bruce and C. P. Grey, *Energy Environ. Sci.*, 2016, **9**, 3240–3251.
23 Nicolas Bucher & Steffen Hartung & Irina Gocheva & and Yan L. Cheah & Madhavi Srinivasan & Harry E. Hoster, *J Solid State Electrochem (2013) 17:1923–1929*, DOI:10.1007/s10008-013-2047-x.
24 A. Konarov, H. J. Kim, N. Voronina, Z. Bakenov and S.-T. Myung, *ACS applied materials & interfaces*, 2019, **11**, 28928–28933.
25 N. Yabuuchi, M. Kajiyama, J. Iwatate, H. Nishikawa, S. Hitomi, R. Okuyama, R. Usui, Y. Yamada and S. Komaba, *Nature Mater*, 2012, **11**, 512–517.

26 W.-L. Pang, X.-H. Zhang, J.-Z. Guo, J.-Y. Li, X. Yan, B.-H. Hou, H.-Y. Guan and X.-L. Wu, *Journal of Power Sources*, 2017, **356**, 80–88.
27 W. Zheng, Q. Liu, Z. Wang, Z. Wu, S. Gu, L. Cao, K. Zhang, J. Fransaer and Z. Lu, *Energy Storage Materials*, 2020, **28**, 300–306.
28 J. H. Jo, H. J. Kim, J. U. Choi, N. Voronina, K.-S. Lee, K. Ihm, H.-K. Lee, H.-D. Lim, H. Kim, H.-G. Jung, K. Y. Chung, H. Yashiro and S.-T. Myung, *Energy Storage Materials*, 2022, **46**, 329–343.
29 A. Konarov, J. H. Jo, J. U. Choi, Z. Bakenov, H. Yashiro, J. Kim and S.-T. Myung, *Nano Energy*, 2019, **59**, 197–206.
30 E. J. Kim, L. A. Ma, L. C. Duda, D. M. Pickup, A. V. Chadwick, R. Younesi, J. T. S. Irvine and A. R. Armstrong, *ACS Appl. Energy Mater.*, 2020, **3**, 184–191.
31 Q. Wang, S. Mariyappan, J. Vergnet, A. M. Abakumov, G. Rousse, F. Rabuel, M. Chakir and J. Tarascon, *Advanced Energy Materials*, 2019, **9**, 1901785.
32 M. Shishkin, S. Kumakura, S. Sato, K. Kubota, S. Komaba and H. Sato, *Chem. Mater.*, 2018, **30**, 1257–1264.
33 X. Rong, E. Hu, Y. Lu, F. Meng, C. Zhao, X. Wang, Q. Zhang, X. Yu, L. Gu, Y.-S. Hu, H. Li, X. Huang, X.-Q. Yang, C. Delmas and L. Chen, *Joule*, 2019, **3**, 503–517.
34 E. J. Kim, T. Hosaka, K. Kubota, R. Tatara, S. Kumakura and S. Komaba, *ACS Appl. Energy Mater.*, 2022, **5**, 12999–13010.
35 J. H. Stansby, N. Sharma and D. Goonetilleke, *J. Mater. Chem. A*, 2020, **8**, 24833–24867.
36 S. F. Linnell, A. G. Manche, Y. Liao, M. Hirsbrunner, S. Imada, A. B. Naden, J. T. S. Irvine, L. C. Duda and A. R. Armstrong, *J. Phys. Energy*, 2022, **4**, 044006.
37 B. Ravel and M. Newville, *J Synchrotron Rad*, 2005, **12**, 537–541.
38 B. Mortemard De Boisse, S. Nishimura, E. Watanabe, L. Lander, A. Tsuchimoto, J. Kikkawa, E. Kobayashi, D. Asakura, M. Okubo and A. Yamada, *Advanced Energy Materials*, 2018, **8**, 1800409.
39 T. Or, K. Kaliyappan, Z. Bai and Z. Chen, *ChemElectroChem*, 2020, **7**, 3284–3290.
40 Y. Liu, C. Wang, M. Ren, H. Fang, Z. Jiang and F. Li, *Journal of Energy Chemistry*, 2021, **63**, 351–357.
41 M. S. Islam and C. A. J. Fisher, *Chem. Soc. Rev.*, 2014, **43**, 185–204.
42 S. Saxena, M. Badole, H. N. Vasavan, V. Srihari, A. K. Das, P. Gami, N. Dagar, S. Deswal, P. Kumar, H. K. Poswal and S. Kumar, *Energy Fuels*, 2024, **38**, 12140–12149.
43 Y. Qiao, S. Guo, K. Zhu, P. Liu, X. Li, K. Jiang, C.-J. Sun, M. Chen and H. Zhou, *Energy Environ. Sci.*, 2018, **11**, 299–305.
44 D. P. Siriwardena, J. F. S. Fernando, T. Wang, K. L. Firestein, C. Zhang, H. E. A. Brand, M. W. M. Jones, C. M. Kewish, P. Berntsen, T. Jenkins, C.-E. M. Lewis, J. E. Von Treifeldt, D. P. Dubal and D. V. Golberg, *Electrochimica Acta*, 2021, **394**, 139139.
45 A. J. Toumar, S. P. Ong, W. D. Richards, S. Dacek and G. Ceder, *Phys. Rev. Applied*, 2015, **4**, 064002.
46 Y.-N. Zhou, P.-F. Wang, Y.-B. Niu, Q. Li, X. Yu, Y.-X. Yin, S. Xu and Y.-G. Guo, *Nano Energy*, 2019, **55**, 143–150.
47 N. Voronina, M. Shin, H. Kim, N. Yaqoob, O. Guillon, S. H. Song, H. Kim, H. Lim, H. Jung, Y. Kim, H. Lee, K. Lee, K. Yazawa, K. Gotoh, P. Kaghazchi and S. Myung, *Advanced Energy Materials*, 2022, **12**, 2103939.
48 D. Eum, B. Kim, J.-H. Song, H. Park, H.-Y. Jang, S. J. Kim, S.-P. Cho, M. H. Lee, J. H. Heo, J. Park, Y. Ko, S. K. Park, J. Kim, K. Oh, D.-H. Kim, S. J. Kang and K. Kang, *Nat. Mater.*, 2022, **21**, 664–672.
49 N. Yabuuchi, M. Nakayama, M. Takeuchi, S. Komaba, Y. Hashimoto, T. Mukai, H. Shiiba, K. Sato, Y. Kobayashi, A. Nakao, M. Yonemura, K. Yamanaka, K. Mitsuhara and T. Ohta, *Nat Commun*, 2016, **7**, 13814.
50 C. Li, C. Zhao, B. Hu, W. Tong, M. Shen and B. Hu, *Chem. Mater.*, 2020, **32**, 1054–1063.
51 M. Jia, H. Li, Y. Qiao, L. Wang, X. Cao, J. Cabana and H. Zhou, *ACS Appl. Mater. Interfaces*, 2020, **12**, 38249–38255.

52 K. Min, K. Kim, C. Jung, S.-W. Seo, Y. Y. Song, H. S. Lee, J. Shin and E. Cho, *Journal of Power Sources*, 2016, **315**, 111–119.
53 Q. Huang, J. Liu, L. Zhang, S. Xu, L. Chen, P. Wang, D. G. Ivey and W. Wei, *Nano Energy*, 2018, **44**, 336–344.
54 C. Cheng, H. Hu, C. Yuan, X. Xia, J. Mao, K. Dai and L. Zhang, *Energy Storage Materials*, 2022, **52**, 10–18.
55 C. Cheng, C. Chen, S. Chu, H. Hu, T. Yan, X. Xia, X. Feng, J. Guo, D. Sun, J. Wu, S. Guo and L. Zhang, *Advanced Materials*, 2022, **34**, 2201152.
56 G. Chen, H. Ji, H. Fang, J. Zhai, Z. Ma, W. Ji, Y. Wang, Y. Huang, L. Liu, W. Tong, W. Zeng and Y. Xiao, *ACS Appl. Mater. Interfaces*, 2023, **15**, 33682–33692.
57 S. Kumakura, Y. Tahara, K. Kubota, K. Chihara and S. Komaba, *Angew Chem Int Ed*, 2016, **55**, 12760–12763.

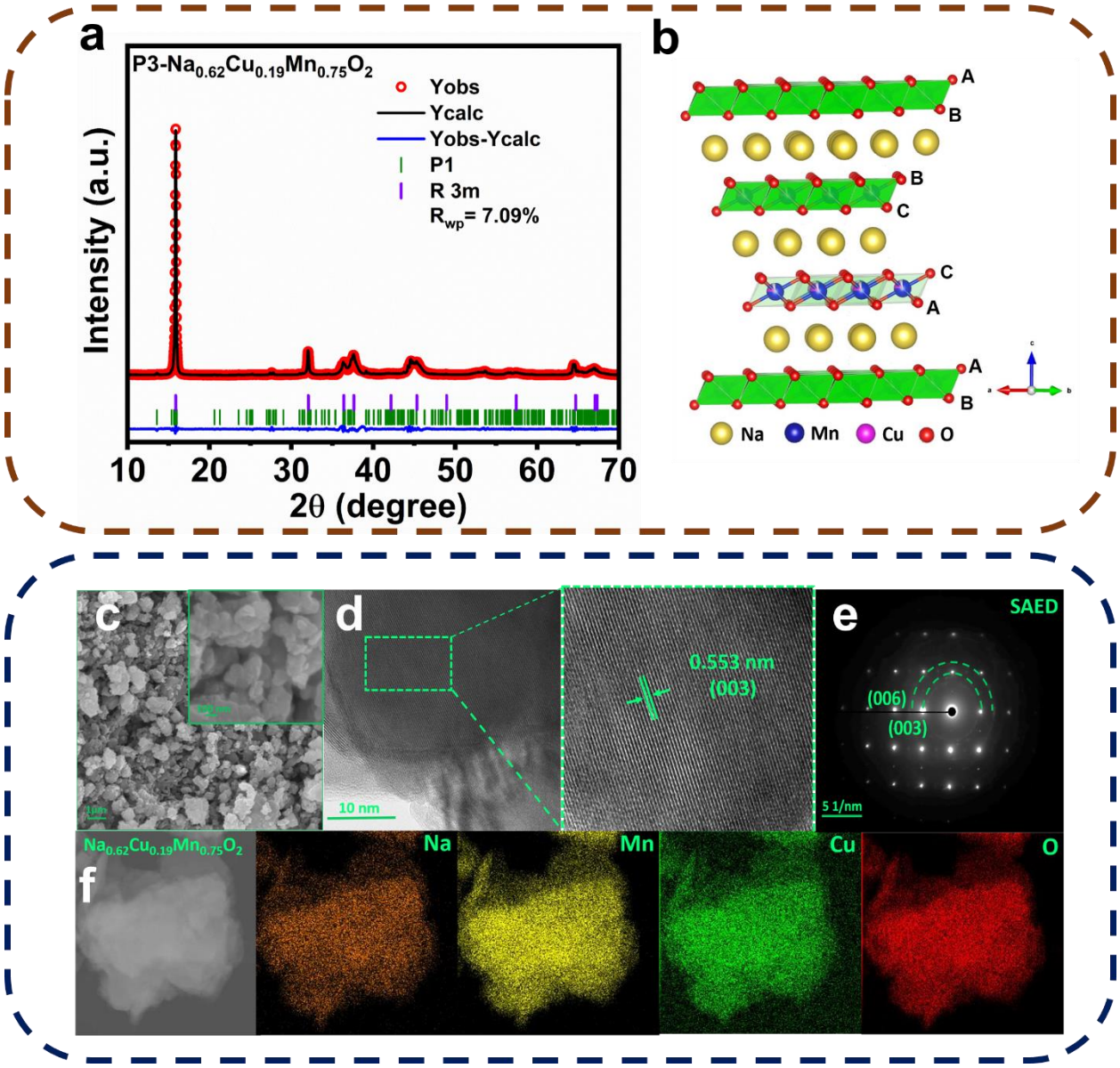

Fig. 1. a) XRD Rietveld refinement of $Na_{0.62}Mn_{0.75}Cu_{0.19}O_2$. b) Crystal structure illustration. c) SEM image. d) HR-TEM images. e) SAED pattern of $Na_{0.62}Mn_{0.75}Cu_{0.19}O_2$, f) TEM EDS mapping.

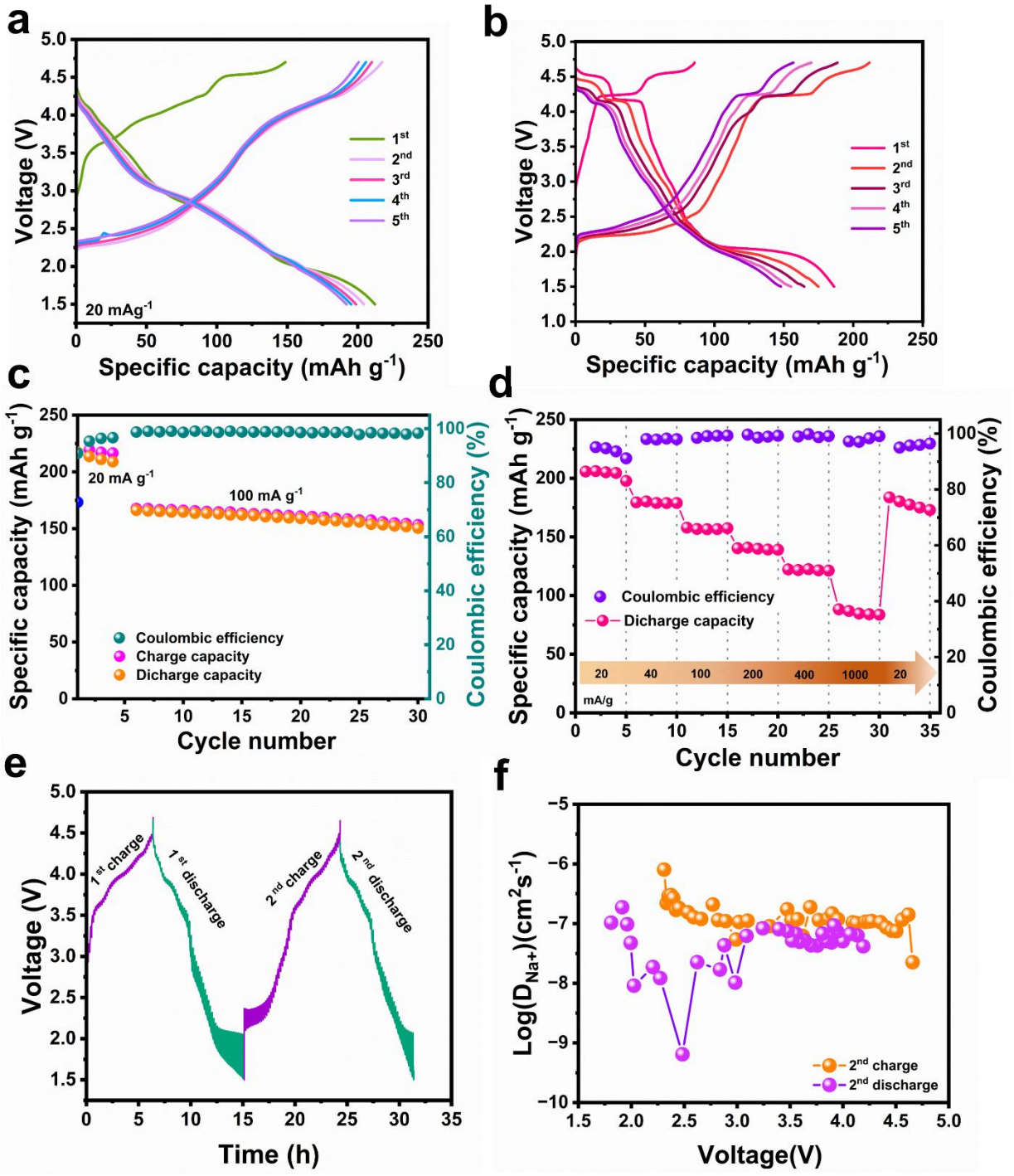

Fig. 2. a) Voltage profiles of $Na_{0.62}Mn_{0.75}Cu_{0.19}O_2$ vs Na between 1.5-4.7 V at 20 mA g^{-1}. b) Voltage profiles of undoped material. c) Cycling performance in two different current rate: 20 mA g^{-1} and 100 mA g^{-1}. d) Rate performance of at different current densities. e) GITT profiles of during the second charge/discharge process. f) Variation of the D_{Na+} values vs potential.

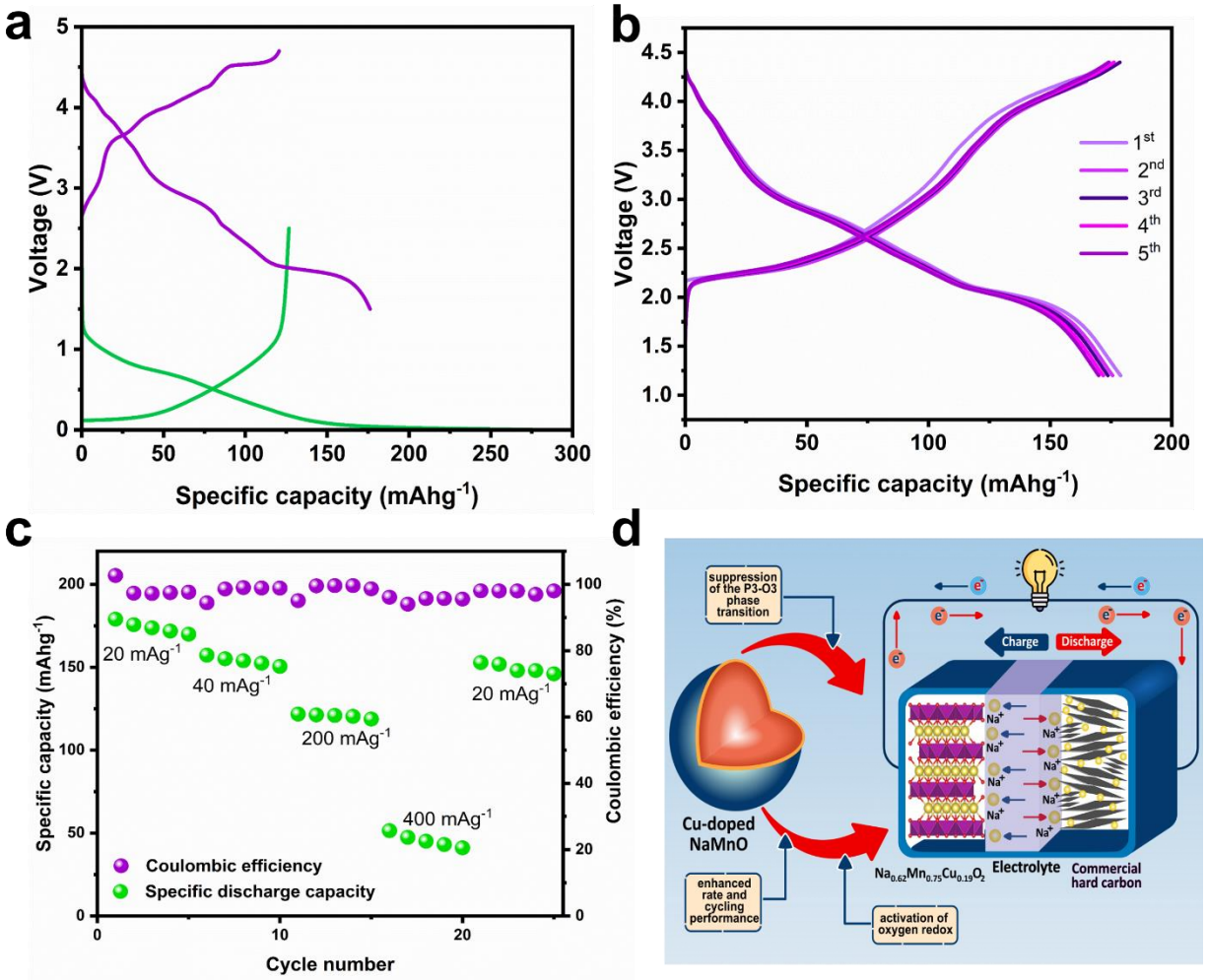

Fig. 3. a) The first charge-discharge curves of the $Na_{0.62}Mn_{0.75}Cu_{0.19}O_2$ and commercial hard carbon. b) Voltage profile of full cell between 1.2- 4.4 V. c). c) Rate performance of full cell at different current densities. d) Schematic illusration of the $Na_{0.62}Mn_{0.75}Cu_{0.19}O_2$ and commercial hard carbon.

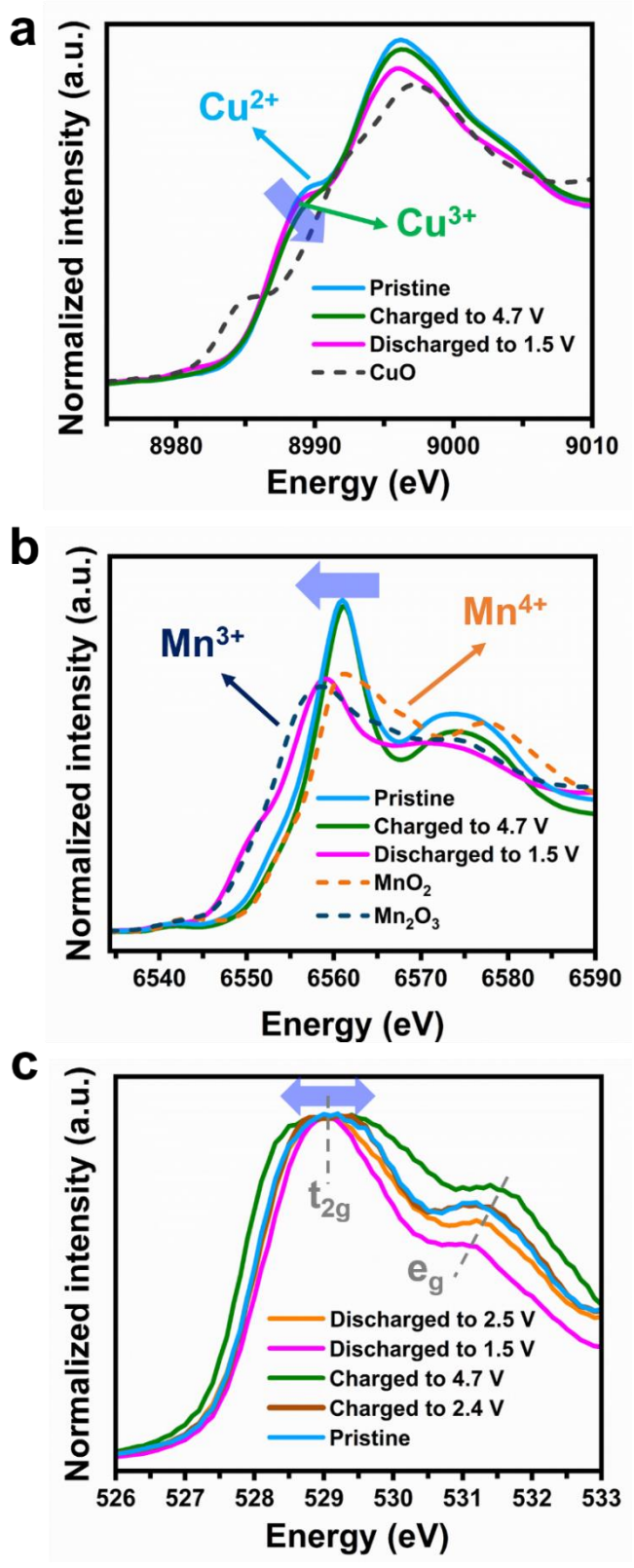

Fig. 4. *Ex situ* XANES spectra of K-edges of a) copper, b) manganese, and c) oxygen.

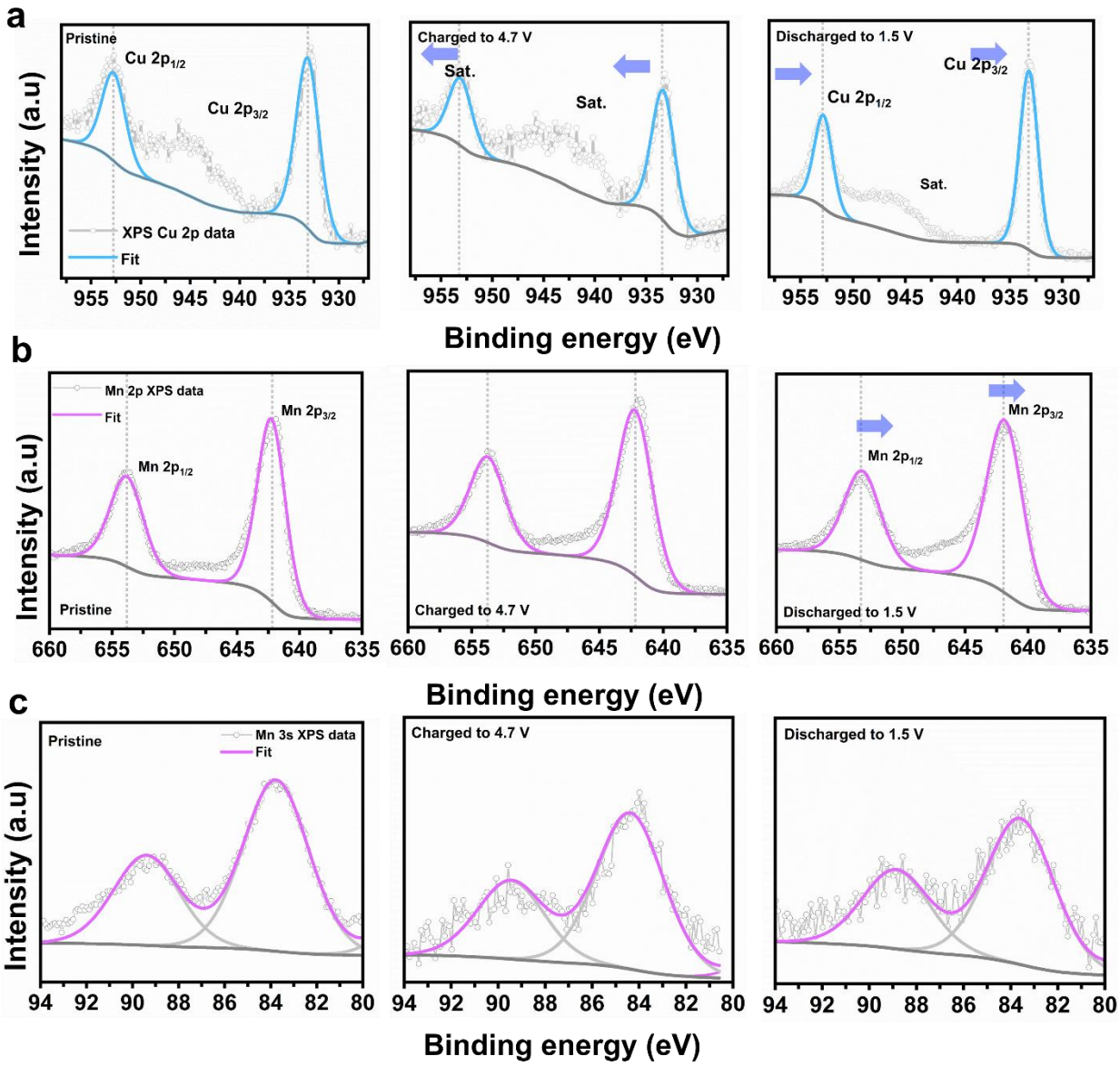

Fig. 5. *Ex situ* XPS spectra of the electrodes a) Cu 2p, b) Mn 2p, c) Mn 3s

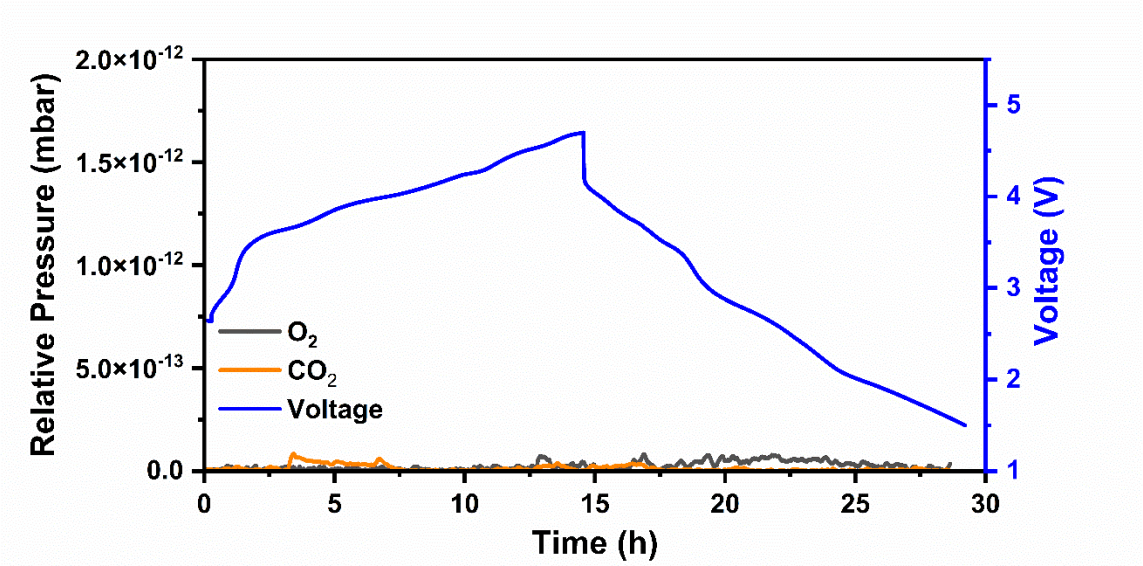

Fig. 6. *Operando* DEMS analysis during the first cycle

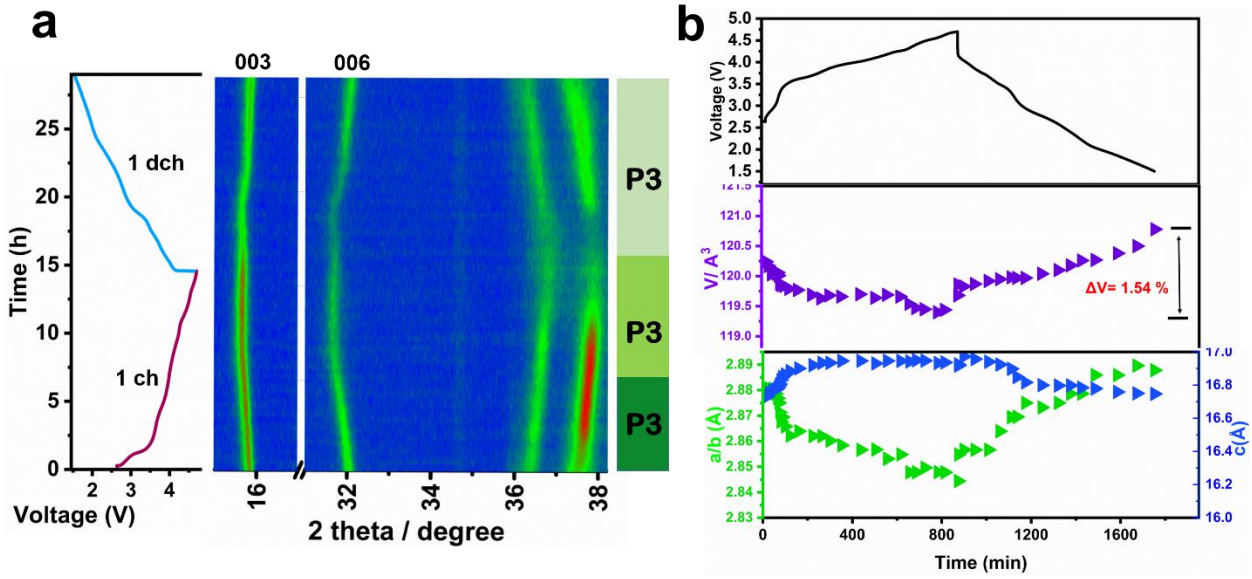

Fig. 7. a) *Operando* XRD patterns of the first charge/discharge at 1.5−4.7 V of $Na_{0.62}Mn_{0.75}Cu_{0.19}O_2$; b) Variation of lattice parameters